



## Nano-architected $\text{CeO}_2$ supported Rh with remarkably enhanced catalytic activity for propylene glycol reforming reaction in microreactors

Vetrivel Shanmugam<sup>a,\*</sup>, Ralf Zapf<sup>a</sup>, Volker Hessel<sup>b</sup>, Helmut Pennemann<sup>a</sup>, Gunther Kolb<sup>a,b,\*</sup>

<sup>a</sup> Fraunhofer ICT-IMM, Division of Energy and Chemical Technology, Carl-Zeiss-Straße 18-20, 55129 Mainz, Germany

<sup>b</sup> Department of Chemical Engineering and Chemistry, Micro Flow Chemistry and Process Technology, Eindhoven University of Technology, P.O. Box 513, 5600 MB Eindhoven, The Netherlands



### ARTICLE INFO

**Keywords:**  
 Ceria  
 Morphology  
 Alumina  
 Rhodium  
 Steam reforming  
 Propylene glycol

### ABSTRACT

The influence of morphology and crystalline facets of nanoshaped ceria oxide support in Rh/ $\text{CeO}_2$  and Rh/ $\text{CeO}_2/\text{Al}_2\text{O}_3$  catalysts have been investigated by oxidative steam reforming of propylene glycol in microreactors at 630 °C at S/C = 3.5 and O/C = 0.15. First, well-defined ceria nanorods (NRs) and nanocubes (NCs) have been successfully synthesized by a facile hydrothermal method and then they are deposited on to  $\alpha\text{-Al}_2\text{O}_3$ . The result of transmission electron microscopy indicates that the ceria nanorods exposed (110) and (100) planes but nanocubes possess only (100) planes. The developed shape controlled ceria nanocrystals and they are mixed with alumina have been used as supports for the preparation of highly dispersed and size controlled Rh nanoparticles of Rh/ $\text{CeO}_2$  and Rh/ $\text{CeO}_2/\text{Al}_2\text{O}_3$  catalysts. Their performance was tested for the propylene glycol reforming reaction in microreactors, which provide high surface of the catalyst coatings, heat and mass transfer rate and controllability. The XPS and TEM results indicate that the  $\text{CeO}_2$  morphology shows the selective exposure of different crystal planes which has a significant impact on the dispersion of Rh nanoparticles that influenced in the reforming reaction. The steam reforming reaction experiments show that the ceria nanorods supported Rh catalyst was achieved significantly better activity and stability for 100 h of time on stream than for the all other catalysts. This could be related to the better dispersion of Rh species and the higher surface oxygen vacancies associated with the exposed (100) and (110) crystal planes favor the stabilization of Rh nanoparticles against sintering and elimination of carbon deposition on active Rh nanoparticles during reforming reaction.

### 1. Introduction

Hydrogen production by steam reforming of polyalcohols has emerged as a promising alternative reaction in recent years. Especially propylene glycol is an attractive fuel for specific mobile applications in the aerospace environment owing to its non-toxicity and inflammability [1]. Because of the oxidative steam reforming is an endothermic catalytic reaction, a microreactor (MR) arranged as plate heat-exchanger is the most efficient and compact reactor design for conducting this reaction on-board a vehicle to circumvent any heat transfer problems through combustion of unconverted hydrogen from the fuel cell anode in the second pass of the heat-exchanger. Owing to the high surface to volume ratio, microreactors achieve high heat and mass transfer rates, good phase contacting and thus seem to be particularly well suited for the production of hydrogen by steam reforming reactions [2–7]. Cai et al. [8] studied the hydrogen production by steam reforming of ethanol in microchannel reactors and concluded that the activity of their catalyst was higher in the case of the microchannel reactors when

comparing their performance with a packed bed reactor. Görke and co-authors [9] investigated the kinetics of steam reforming of ethanol in microreactors and confirmed that the performance of their catalyst was not affected by mass and heat transfer resistances.

In order to achieve high fuel conversion and high hydrogen yield through the application of microreactors, highly active and stable catalyst is required. Among the noble and non-noble metal catalysts studied to date, rhodium has been found to be one of the most suitable metal for the steam reforming reaction of hydrocarbons and higher (poly)alcohols [10–12], as it shows the highest stability, activity and selectivity towards hydrogen due to its capability to break the C–C bond [13]. Most importantly, the catalyst support materials should generally possess adequate chemical and mechanical properties to provide the required stability under the steam reforming conditions at high temperatures. From the viewpoint of increasing advantages, ceria is an important support material for promoting the dispersion of the active metal nanoparticles and increasing the metal–support interaction which can enhance the catalytic performance in reforming reactions

\* Corresponding authors at: Fraunhofer ICT-IMM, Division of Energy and Chemical Technology, Carl-Zeiss-Straße 18–20, 55129 Mainz, Germany.  
 E-mail addresses: [vetrivel.shanmugam@imm.fraunhofer.de](mailto:vetrivel.shanmugam@imm.fraunhofer.de) (V. Shanmugam), [Gunther.kolb@imm.fraunhofer.de](mailto:Gunther.kolb@imm.fraunhofer.de) (G. Kolb).

[14–17]. Moreover, ceria can improve the catalyst stability due to its high oxygen storage capacity (OSC) and the oxygen exchange capacity, which is associated with its ability to reversibly change oxidation states between  $\text{Ce}^{4+}$  and  $\text{Ce}^{3+}$  [18,19]. Recently, we reported that the easily accessible oxygen from  $\text{CeO}_2$  can react and eliminate the carbon species as soon as it forms and this process keeps the active metal surface free of carbon, thus inhibiting deactivation [20]. Thormann [21] et al. examined the hexadecane reforming in a microchannels coated with Rh/ $\text{CeO}_2$  catalyst and observed the significant impact of the ceria support on the reformate composition. Steam reforming of ethanol was studied over Rh/ $\text{CeO}_2/\text{Al}_2\text{O}_3$  catalysts in a microchannel reactor and their results are compared with the performance of a packed bed reactor [22]. No carbon formation was observed on the Rh/ $\text{CeO}_2$  during dry methanol reforming due to a higher surface fugacity of oxygen species adsorbed on the ceria support that react to remove carbon [23]. Montini et al. [24] synthesized the Rh@ $\text{Ce}_x\text{Zr}_{1-x}\text{O}_2-\text{Al}_2\text{O}_3$  nanocomposites by direct sol-gel method for efficient hydrogen production from ethanol steam reforming reaction. The authors reported that the presence of ceria-zirconia mixed oxides in the nanocomposites play a key role to reduce carbon formation and facilitate its removal. Recently, Roh et al. [25] reported that Rh/ $\text{CeO}_2-\text{ZrO}_2$  is very active for ethanol steam reforming and the supports favor the oxidation of carbonaceous species. The  $\text{CeO}_2$  addition to  $\text{Al}_2\text{O}_3$  support shows distinct impact on the catalytic activity of Rh catalysts for steam reforming of propane [26]. The addition of ceria stabilizes the structure of alumina by forming  $\text{CeAlO}_3$  and to maintain the dispersion of rhodium [18].

However, the structure-sensitive behavior of shape controlled ceria oxide has attracted significant attention owing to its unique catalytic properties, and fruitful results have been achieved in catalytic applications [27–30]. For example, the crystal facets of the  $\text{CeO}_2$  support play an important role in dispersion of active metal and stabilization of metal particles against sintering under high temperature reaction condition. In general,  $\text{CeO}_2$  nanorods preferentially expose four (110) and two (100) planes, while the  $\text{CeO}_2$  nanocubes expose six (100) planes [31]. According to the theoretical calculations, the surface energy and catalytic activity indicate that the (110) and (100) faces are more active, which means to increase the fraction of reactive (110) and (100) planes, than the (111) planes of  $\text{CeO}_2$  nanoparticles [32–35]. On the other hand, ceria nanorods and nanocubes exhibit a greater capacity to store oxygen than ceria nanoparticles that could resist the carbon deposition on active metal. The effect of the morphology of nanocrystalline  $\text{CeO}_2$  supported Rh catalyst was studied on the ethanol reforming reaction [27,36,37]. The influence of nano-architected  $\text{CeO}_2$  supports in RhPd/ $\text{CeO}_2$  for the catalytic ethanol steam reforming reaction was reported by Divins et al. [38]. The crystal plane effect of  $\text{CeO}_2$  nanostructures on the catalytic activity of Ni/ $\text{CeO}_2$  and Ru/ $\text{CeO}_2$  has been studied on different reactions [39,30]. The morphology effect of  $\text{CeO}_2$  catalyst is mainly dependent on the reaction system and the nature of the metal dispersed on the  $\text{CeO}_2$  support. For example, the catalysts based on  $\text{CeO}_2$  nanorods were more active and selective in NO reduction [40] and CO oxidation [41,42], while catalysts based on  $\text{CeO}_2$  nanocubes exhibit superior properties in soot combustion [43] and hydrogen oxidation [44]. Moraes et al. [45] and Soykal et al. [36] found that ceria nanocube possess good reducibility and oxygen mobility and improved the dispersion of metals, leading to superior performance of steam reforming of ethanol. Rh/ $\text{CeO}_2$  catalysts with  $\text{CeO}_2$  nanocrystals of rod and cubic shape exhibit satisfactory catalytic activity on steam reforming of ethanol [27]. Wang et al. [28] reported that Ni/ $\text{CeO}_2$  nanorods exhibited excellent catalytic behavior in catalytic activity in methane dry reforming. Although many works have been reported on the catalytic activity of nanoshaped  $\text{CeO}_2$  supported catalysts in reforming reaction [27,28,36–39], there is no report dealing with the effect of  $\text{CeO}_2$  morphology on the catalytic performance in the reforming of propylene glycol in microreactors. We here present the influence of the morphology and crystal plane of ceria for the first time on catalytic efficiency of steam reforming of propylene

glycol in microreactors and discussed the role of crystal plane and oxygen vacancy in ceria.

## 2. Experimental

### 2.1. Catalyst preparation

Shape controlled  $\text{CeO}_2$  nanorods and nanocubes were prepared by a facile hydrothermal method as reported previously [30]. First, 3.47 g of  $\text{Ce}(\text{NO}_3)_3 \cdot 6\text{H}_2\text{O}$  dissolved in 40 mL of deionized water. Then, 38.4 g of NaOH dissolved in 120 mL of water were added into ceria solution and stirred for 15 min for the formation of a milky suspension. Subsequently, the suspension was transferred into a Teflon-lined stainless steel autoclave and then the autoclave was sealed and heated for 24 h at 100 °C for NRs and 180 °C for NCs. After the hydrothermal treatment, the precipitates were separated by centrifugation process. Then, the precipitates were re-suspended in water under ultra-sonication for 10 min, and then separated again using centrifugation. This process was repeated three times. The solids were then washed in ethanol and recovered by centrifugation using the same procedure, which was also repeated three times to remove completely possible sodium ionic remnants. The solids obtained were dried at 100 °C overnight and then calcined at 450 °C for 5 h in presence of air. 20% of obtained  $\text{CeO}_2$  nanocrystals were mixed with  $\alpha-\text{Al}_2\text{O}_3$  in aqueous medium and stirred for 3 h. The mixtures were dried at 100 °C for 12 h and followed by calcination at 450 °C for 5 h. For comparison, the  $\text{CeO}_2/\text{Al}_2\text{O}_3$  was also prepared by direct impregnation of  $\text{Ce}(\text{NO}_3)_3 \cdot 6\text{H}_2\text{O}$  precursor on to  $\alpha-\text{Al}_2\text{O}_3$  and the solids were dried at 100 °C for 12 h and calcined at 450 °C for 5 h in air. Subsequently, 5 wt% of Rh was impregnated separately on to  $\text{CeO}_2$  and  $\text{CeO}_2/\text{Al}_2\text{O}_3$  using  $\text{RhCl}_3 \cdot x\text{H}_2\text{O}$  as a precursor and calcined at 450 °C for 3 h. The catalysts prepared are hereafter denoted as Rh/ $\text{CeO}_2$ –NR, Rh/ $\text{CeO}_2$ –NC, Rh/ $\text{CeO}_2$ –NR/ $\text{Al}_2\text{O}_3$ , Rh/ $\text{CeO}_2$ –NC/ $\text{Al}_2\text{O}_3$  and Rh/ $\text{CeO}_2$ / $\text{Al}_2\text{O}_3$  (prepared by direct impregnation of ceria on alumina). The quantitative analysis of Rh and Ce was determined by XRF and their results are presented in the results and discussion Section 3.1. The obtained catalysts were coated onto microchannels of stainless steel microreactors by applying our previously reported wash coating technique [20,46].

### 2.2. Catalyst characterization

The TEM images were acquired on a FEI Tecnai microscope operating at 200 kV. For TEM observations, the catalyst samples were coated into the copper grids by suspending a small amount of the catalyst in ethanol under ultra-sonication (Branson, 100 W42 kHz) for 1 h. A drop of catalyst suspension was then placed on to the copper grids with holey carbon films, followed by drying at room temperature. Rigaku multipurpose X-ray diffraction instrument with Ni-filtered  $\text{Cu K}\alpha$  radiation was used to collect the powder X-ray diffraction (XRD) patterns. XPS measurements were carried out on a Thermo Scientific K-Alpha spectrometer equipped with a monochromatic small-spot X-ray source and a 180° double focusing hemispherical analyzer with a 128-channel delay line detector. Spectra were obtained for all the calcined catalyst using an aluminum anode ( $\text{AlK}\alpha = 1486.6$  eV) operated at 72 W and a spot size of 400  $\mu\text{m}$ . Survey scans were measured at constant pass energy of 200 eV, and high-resolution scans of the separate regions were measured at 50 eV. The background pressure of the ultra-high vacuum (UHV) chamber was  $2 \times 10^{-8}$  mbar. All of the binding energies that are reported have been calibrated to the C 1 s transition at 284.5 eV. The surface area of all catalysts was measured at 77 K on a Micromeritics Tristar II analyzer. The catalysts were degassed at 150 °C for 2 h before measurements. The Brunauer-Emmett-Teller (BET) method in the relative pressure range of  $P/P_0 = 0.0–0.4$  was employed to obtain specific surface areas. The  $\text{H}_2$ -TPR measurements were carried out for calcined catalysts in a quartz tube reactor equipped with a thermal conductivity detector (TCD). The catalysts were

pretreated at 300 °C for 60 min by pulsing of O<sub>2</sub> in an Ar flow, then purged with Ar at 500 °C for 15 min and cooled to room temperature. 10% H<sub>2</sub> of N<sub>2</sub> gas mixture (25 mL/min) was introduced and the programming temperature was controlled from room temperature to 750 °C with a rate of 10 °C/min. The TPO measurements were carried out for used catalysts with the same procedure of H<sub>2</sub>-TPR. The difference was that 10% O<sub>2</sub> in N<sub>2</sub> gas mixture was applied as carrier gas. Carbon deposition was quantified on used catalysts using Perkin Elmer TGA7 thermogravimetric analyzer (TGA) with a heating rate of 10 °C/min under air in a flow of 50 mL/min.

### 2.3. Catalytic activity measurements

Oxidative steam reforming test was carried out in a plug flow-type apparatus with a microchannel reactor at atmospheric pressure, temperature at 630 °C and WHSV of 94 L g<sup>-1</sup> h<sup>-1</sup>. The mixture of water and propylene glycol (S/C = 3.5) was placed in a tank under inert gas pressure as driving force for feeding a liquid mass flow controller (LMFC), and using an evaporator, the mixture was introduced into the test reactor. The test reactor has a sandwich design with two microchannel platelets being attached face to face. Each platelet carries 14 channels of 25 mm long, 500 μm wide and 250 μm deep. A pair of platelets was coated with developed catalysts and subsequently sealed by laser welding [47,48]. Inlet and outlet capillaries were attached to the microchannel reactors by laser welding as well. A synthetic air stream was added by a gas MFC to the previously vaporized propylene glycol-water mixture in order to reach an intended atomic oxygen to carbon (O/C) ratio of 0.15. The total flow rate of vapor was 30 mL/min. Before starting the experiment, the reactor was by-passed until a stable feed composition and the desired reactor temperature were reached. The wash coated catalysts were pre reduced in 20% H<sub>2</sub>/N<sub>2</sub> at 500 °C for 2 h prior to the catalytic test. The obtained product composition was analyzed by on-line Gas Chromatograph (Thermo Scientific) consisting of two TCD and one FID detectors.

## 3. Results and discussion

### 3.1. Characteristics of catalysts

The crystal structures of ceria and alumina in Rh/CeO<sub>2</sub>-NR, Rh/CeO<sub>2</sub>-NC, Rh/CeO<sub>2</sub>-NR/Al<sub>2</sub>O<sub>3</sub>, Rh/CeO<sub>2</sub>-NC/Al<sub>2</sub>O<sub>3</sub> and Rh/CeO<sub>2</sub>/Al<sub>2</sub>O<sub>3</sub> catalysts were investigated by wide-angle XRD and their results are shown in Fig. 1. Each spectrum exhibited the diffraction reflections at 28.3°, 33°, 47.3°, 56.2° and 58.9° corresponding to (111), (200), (220), (311) and (222) planes are ascribed to the fluorite structure of ceria, while no reflections corresponding to Rh species were observed in any of the samples, indicating high dispersion of Rh nanoparticles. The absence of Rh reflections indicating that small size (< 5 nm) Rh species were present in the calcined catalysts, which is largely undetectable by XRD [16]. This result is consistent with the dispersion and size of Rh nanoparticle estimated by TEM measurement as discussed below. In Rh/CeO<sub>2</sub>-NR/Al<sub>2</sub>O<sub>3</sub>, Rh/CeO<sub>2</sub>-NC/Al<sub>2</sub>O<sub>3</sub> and Rh/CeO<sub>2</sub>/Al<sub>2</sub>O<sub>3</sub> samples, except CeO<sub>2</sub> reflections the rest of additional peaks appeared at 25.5°, 35.1°, 43.3° and 57.4° corresponding to characteristic planes of (012), (104), (113) and (116) of α-Al<sub>2</sub>O<sub>3</sub>, demonstrating that the α-Al<sub>2</sub>O<sub>3</sub> is a relatively pure phase. By using the Scherrer equation of XRD pattern, the crystallite size of CeO<sub>2</sub> NRs and NCs calculated from CeO<sub>2</sub> (111) reflection of Rh/CeO<sub>2</sub>-NR and Rh/CeO<sub>2</sub>-NC catalysts was about ca. 29 and 33 nm respectively. There was no change observed on crystal size of CeO<sub>2</sub> NRs and NCs after they were loaded on to alumina. When ceria was directly impregnated on to alumina the (111) plane of CeO<sub>2</sub> became broader and decreased in intensity, indicating the formation of smaller grain size. The size of CeO<sub>2</sub> nanoparticles resulting from the precipitation on alumina is about ca. 15.6 nm. The surface area that were obtained from the N<sub>2</sub> adsorption-desorption measurements is 37.5, 20.8 and 29.4 m<sup>2</sup>/g, respectively for CeO<sub>2</sub> NRs, CeO<sub>2</sub> NCs and

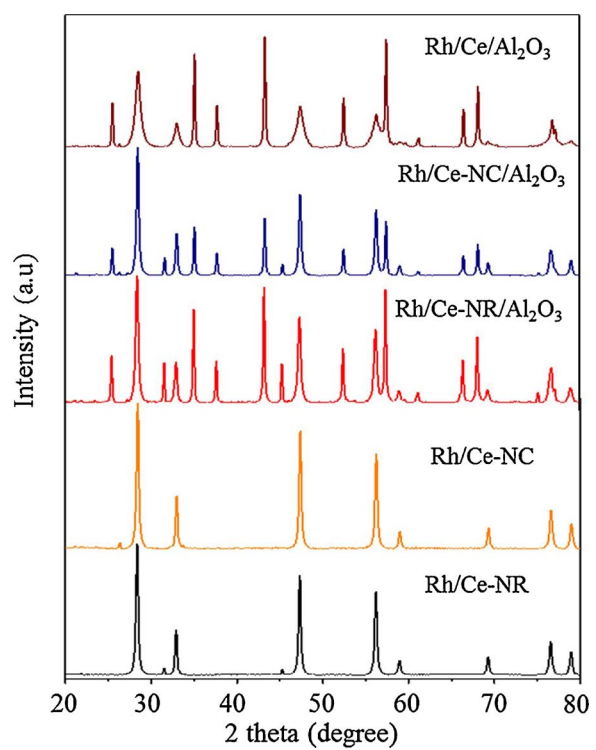


Fig. 1. Wide-angle XRD of calcined catalysts.

CeO<sub>2</sub>/Al<sub>2</sub>O<sub>3</sub>. The Rh content was determined by XRF to 4.56%, 4.61%, 4.37%, 4.38% and 4.21%, respectively for Rh/CeO<sub>2</sub>-NR, Rh/CeO<sub>2</sub>-NC, Rh/CeO<sub>2</sub>-NR/Al<sub>2</sub>O<sub>3</sub>, Rh/CeO<sub>2</sub>-NC/Al<sub>2</sub>O<sub>3</sub> and Rh/CeO<sub>2</sub>/Al<sub>2</sub>O<sub>3</sub> catalysts.

XPS was employed to investigate the chemical state of ceria nanostructures for Rh/CeO<sub>2</sub>-NR, Rh/CeO<sub>2</sub>-NC, Rh/CeO<sub>2</sub>-NR/Al<sub>2</sub>O<sub>3</sub>, Rh/CeO<sub>2</sub>-NC/Al<sub>2</sub>O<sub>3</sub> and Rh/CeO<sub>2</sub>/Al<sub>2</sub>O<sub>3</sub> catalysts. XPS spectra of nanostructured CeO<sub>2</sub> and CeO<sub>2</sub>/Al<sub>2</sub>O<sub>3</sub> supported Rh catalysts are shown in Fig. 2. The two groups of spin-orbit multiplets are labeled as u and v in Fig. 2A attributed to coupling of 3d<sub>3/2</sub> and 3d<sub>5/2</sub> respectively. The peaks indicated as u and v, u<sub>2</sub> and v<sub>2</sub>, and u<sub>3</sub> and v<sub>3</sub> are assigned to a mixture of Ce IV (3d<sup>9</sup>4f<sup>2</sup>) O (2p<sup>4</sup>), Ce IV (3d<sup>9</sup>4f<sup>1</sup>) O (2p<sup>5</sup>), and Ce IV (3d<sup>9</sup>4f<sup>0</sup>) O (2p<sup>6</sup>), respectively, while the peaks u<sub>1</sub> and v<sub>1</sub> are attributed to a mixture of Ce III (3d<sup>9</sup>4f<sup>2</sup>) O (2p<sup>5</sup>) and Ce III (3d<sup>9</sup>4f<sup>1</sup>) O (2p<sup>6</sup>), respectively [26]. As a result, the surface of cerium for all the catalysts is mainly in +4 oxidation state, and a small part of Ce<sup>3+</sup> co-exists. The Rh 3d XP spectra of Rh/CeO<sub>2</sub>-NR, Rh/CeO<sub>2</sub>-NC, Rh/CeO<sub>2</sub>-NR/Al<sub>2</sub>O<sub>3</sub> and Rh/CeO<sub>2</sub>-NC/Al<sub>2</sub>O<sub>3</sub> catalysts showed a doublet centered at around 309 and 314 eV as shown in Fig. 2B. The BE of Rh 3d<sub>3/2</sub> and 3d<sub>5/2</sub> for Rh/CeO<sub>2</sub>-NR and Rh/CeO<sub>2</sub>-NC is 313.7 and 308.8 eV, suggest that rhodium in the +3 oxidation state. When CeO<sub>2</sub> impregnated directly on to Al<sub>2</sub>O<sub>3</sub> the Rh signals increased significantly can be attributed to the large particle size of Rh clusters on CeO<sub>2</sub> and Al<sub>2</sub>O<sub>3</sub>. XPS results of O 1 s core electron levels for all the catalysts are shown in Fig. 2C. The spectrum of Rh/CeO<sub>2</sub>-NR and Rh/CeO<sub>2</sub>-NC shows a peak at 529.1 eV which can be attributed to the lattice oxygen in CeO<sub>2</sub>, and a shoulder appeared on the high BE side (531.1 eV) which corresponds to weakly bonded oxygen species and/or chemisorbed oxygen; the highest binding energy (532.7 eV) corresponded to the surface absorbed oxygen or oxygen species in the surface hydroxyl groups [49]. In the case of Rh/CeO<sub>2</sub>-NR/Al<sub>2</sub>O<sub>3</sub> and Rh/CeO<sub>2</sub>-NC/Al<sub>2</sub>O<sub>3</sub> catalysts, the main peak appeared at 531.1 eV, which could be considered as a combination of the oxygen from Al<sub>2</sub>O<sub>3</sub>, CeO<sub>2</sub> and adsorbed oxygen. However, the fitting curves show that there is small amount of lattice oxygen and adsorbed oxygen due the presence of 20% CeO<sub>2</sub> NRs and NCs on the alumina. No lattice peak was observed for the Rh/CeO<sub>2</sub>/Al<sub>2</sub>O<sub>3</sub> catalyst except the main peak which appeared at higher BE 531.8 eV which means the

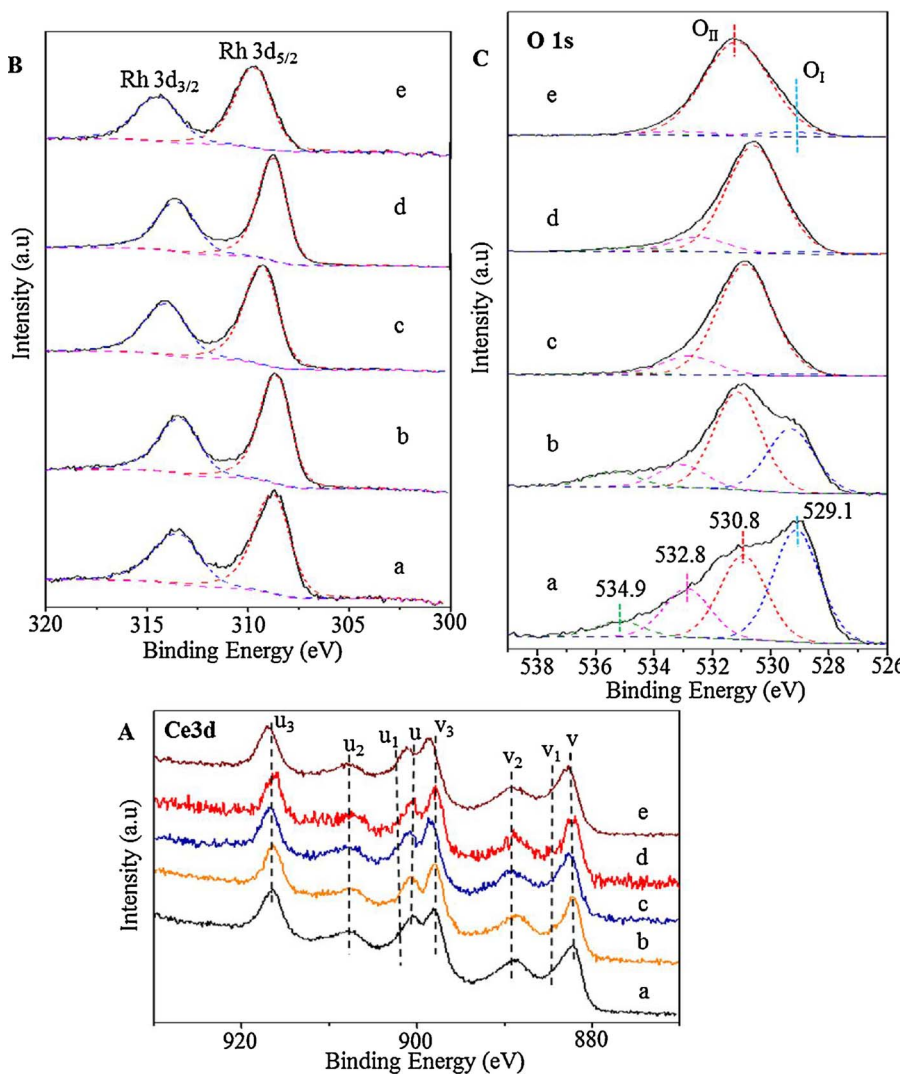


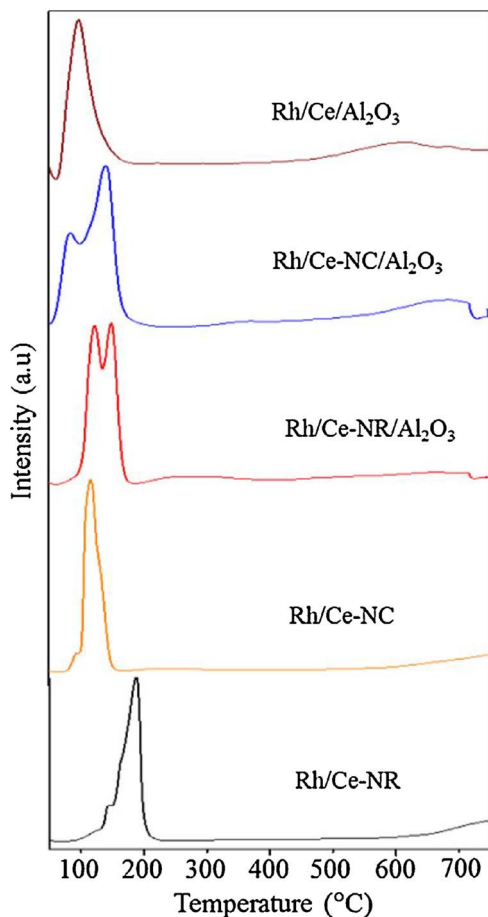
Fig. 2. XPS (A) Ce 3d, (B) Rh 3d and (C) O 1s spectra (a) Rh/CeO<sub>2</sub>-NR, (b) Rh/CeO<sub>2</sub>-NC, (c) Rh/CeO<sub>2</sub>-NR/Al<sub>2</sub>O<sub>3</sub>, (d) Rh/CeO<sub>2</sub>-NC/Al<sub>2</sub>O<sub>3</sub> and (e) Rh/CeO<sub>2</sub>/Al<sub>2</sub>O<sub>3</sub> catalysts.

contribution of the oxygen from CeO<sub>2</sub> decreased and that from Al<sub>2</sub>O<sub>3</sub> increased. This result suggests that the morphology of CeO<sub>2</sub> NRs and NCs effectively influence the active oxygen sites by chemisorbed and adsorbed oxygen on the surface. Moreover, the presence of a higher amount of lattice oxygen indicates the formation of oxygen vacancies which are very important in the catalytic reactions.

The H<sub>2</sub>-TPR profiles for various catalysts used in this study are shown in Fig. 3. As can be seen in this Figure, Rh/CeO<sub>2</sub>-NR catalyst exhibits a sharp H<sub>2</sub> consumption peak at ca. 187 °C, which can be attributed to the reduction of Rh<sub>2</sub>O<sub>3</sub> [50]. In addition, a small shoulder appeared at ca. 142 °C could be assigned to the reduction of isolated Rh<sub>2</sub>O<sub>3</sub> species. The H<sub>2</sub> consumption peaks are slightly shifted to lower temperature for Rh/CeO<sub>2</sub>-NC indicating an easier reduction of rhodium oxides species present. With the addition of CeO<sub>2</sub> NRs and NCs on to Al<sub>2</sub>O<sub>3</sub> in Rh/CeO<sub>2</sub>-NR/Al<sub>2</sub>O<sub>3</sub> and Rh/CeO<sub>2</sub>-NC/Al<sub>2</sub>O<sub>3</sub> catalysts, the shoulder H<sub>2</sub> consumption becomes more pronounced suggesting that the presence of isolated Rh<sub>2</sub>O<sub>3</sub> species is considerably higher in these catalysts and their strength of interaction with the support decreased due to the poor contact between ceria nanocrystals and alumina oxide support. However, when the CeO<sub>2</sub> was directly impregnated on to Al<sub>2</sub>O<sub>3</sub> a single reduction peak was observed at 96 °C for Rh/CeO<sub>2</sub>/Al<sub>2</sub>O<sub>3</sub> due to bulk deposition of Rh<sub>2</sub>O<sub>3</sub> on to ceria or alumina with weak metal-support interaction [51].

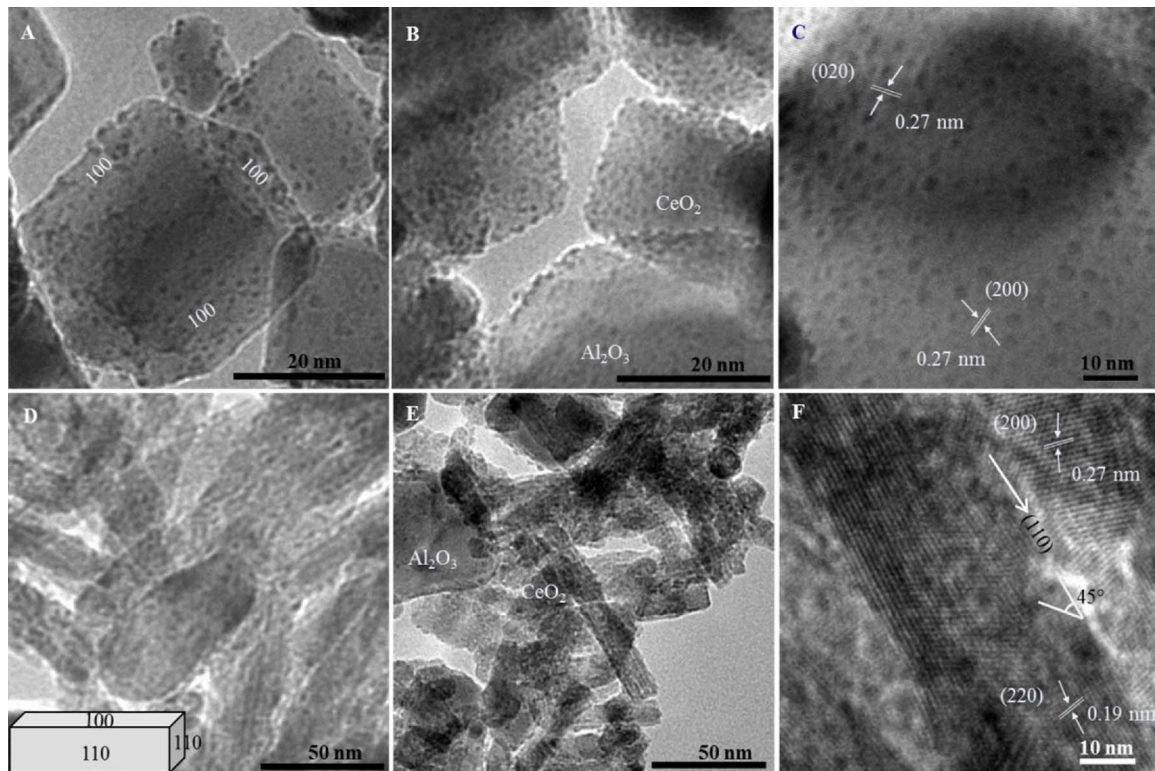
Fig. 4 displays the TEM image of morphology controlled Rh/CeO<sub>2</sub> and Rh/CeO<sub>2</sub>/Al<sub>2</sub>O<sub>3</sub> nanomaterials. Fig. 4A–C shows a smooth surface and uniform size distribution of CeO<sub>2</sub> of perfect cubic shape with an

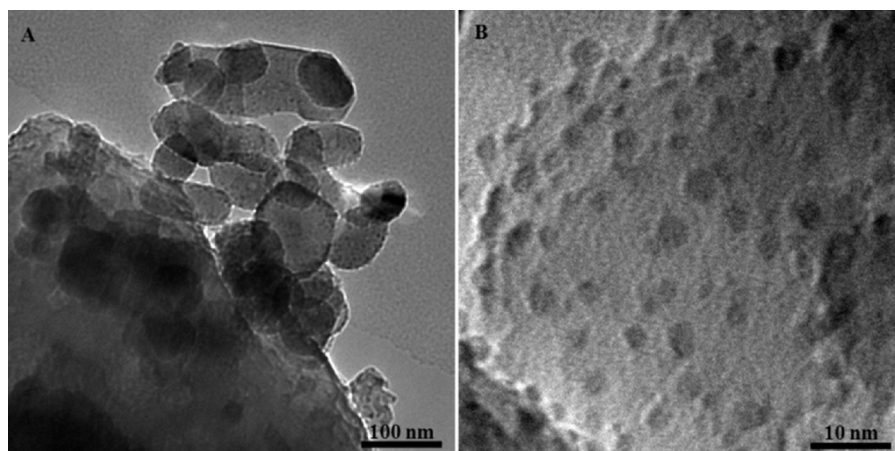
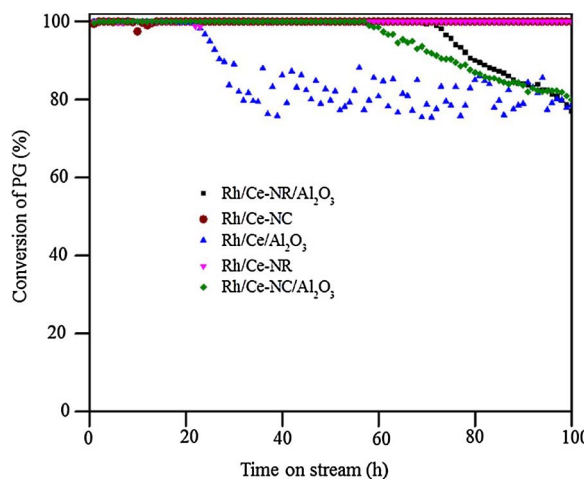
average size of ca. 33 nm. The TEM images of morphology controlled CeO<sub>2</sub> are presented in Fig. S1. As seen in the TEM images, the interplanar d-spacing 0.27 nm is attributed to (200) and (020) planes, indicating preferred growth in the direction along [100] [28,29]. The plane-intersecting angle was 90°. The morphology of most of the CeO<sub>2</sub> NCs was compatible with a cube enclosed by six {100} planes [28]. It is obvious that size controlled Rh nanoparticles uniformly distributed throughout the CeO<sub>2</sub> NCs. Rh/CeO<sub>2</sub>-NC/Al<sub>2</sub>O<sub>3</sub> also shows the homogeneous distribution of Rh nanoparticles both on CeO<sub>2</sub> NCs and Al<sub>2</sub>O<sub>3</sub>. The SEM-EDX spectra confirmed the existence of Rh nanoparticles on CeO<sub>2</sub> NCs and CeO<sub>2</sub>-NC/Al<sub>2</sub>O<sub>3</sub> (Fig. S2 and S3). As can be seen in Fig. 4D–F, the CeO<sub>2</sub> NRs displayed a uniform diameter of ca. 11.5 nm and lengths in the range ca. 60–150 nm, and the lattice fringe directions attributed to (200) and (220) planes with an inter-plane spacing of 0.27 and 0.19 nm, respectively. The CeO<sub>2</sub> NRs grew along the direction of [110], which is predominantly exposed the well-defined plane [110] (located as two side facets and two cross-sectional facets) and [100] plane (located in two side of facets). The TEM images prove that both the CeO<sub>2</sub> NRs and NCs maintained their original crystal shapes and size after depositing them on to alumina and subsequent loading of Rh nanoparticles and followed by heat treatments. In contrast, the irregular shaped CeO<sub>2</sub> nanoparticles aggregated on the alumina surface when they are directly impregnated on alumina (Fig. 5A). However, the distribution of Rh nanoparticles is homogeneous (Fig. 5B).

Fig. 3.  $\text{H}_2$ -TPR profile of calcined catalysts.

### 3.2. Catalytic stability test in oxidative steam reforming reaction

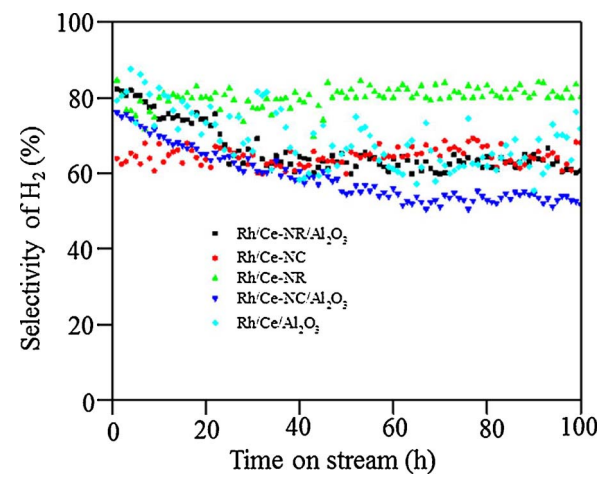
The catalytic performance of all the developed catalysts studied during the oxidative steam reforming of propylene glycol in micro-reactors was evaluated in terms of propylene glycol conversion and product distribution as a function of time on stream. Fig. 6 shows the conversion profiles of steam reforming of propylene glycol (PG) over Rh/CeO<sub>2</sub>-NR, Rh/CeO<sub>2</sub>-NC, Rh/CeO<sub>2</sub>-NR/Al<sub>2</sub>O<sub>3</sub>, Rh/CeO<sub>2</sub>-NC/Al<sub>2</sub>O<sub>3</sub> and Rh/CeO<sub>2</sub>/Al<sub>2</sub>O<sub>3</sub> catalysts at 630 °C with a S/C ratio of 3.5. The PG conversion and product selectivity changed significantly with respect to the CeO<sub>2</sub> morphology. It can be seen that the CeO<sub>2</sub> NRs and CeO<sub>2</sub> NCs supported Rh catalysts show highest stability and higher hydrogen selectivity compared to the all other catalysts. The maximum conversion of PG was 100% over both the Rh/CeO<sub>2</sub>-NR and Rh/CeO<sub>2</sub>-NC catalysts. Notably, the conversion remains complete during 100 h of reaction time for both the catalysts, which exhibits the excellent stability and resistance against sintering of Rh nanoparticles and coke formation. The superior performance in PG conversion over these catalysts may be due to a combination of higher dispersed Rh particles of small size, ease of reducibility and higher oxygen mobility. Rh/CeO<sub>2</sub>-NR/Al<sub>2</sub>O<sub>3</sub> and Rh/CeO<sub>2</sub>-NC/Al<sub>2</sub>O<sub>3</sub> exhibits the constant conversion for a maximum duration of 70 and 60 h, respectively, followed by a deactivation period. The possible reason is that the major portion of Al<sub>2</sub>O<sub>3</sub> support present in these catalysts underwent the lack of mobility of oxygen for 100 h of reaction time and that could deactivate the catalysts by sintering of Rh nanoparticles leading to a reduced stability and incomplete conversion of PG. Comparatively, the Rh/CeO<sub>2</sub>-NR/Al<sub>2</sub>O<sub>3</sub> shows a slightly higher stability than Rh/CeO<sub>2</sub>-NC/Al<sub>2</sub>O<sub>3</sub> originating possibly from a higher dispersion of Rh nanoparticles and mobility of oxygen. The theoretical calculation predicted that the formation of oxygen vacancies on the CeO<sub>2</sub> (110) plane is much more favorable than (100) plane [52]. In addition, the oxygen vacancies formed in (110) plane makes the movement of oxygen atoms in the lattice easier that favor the stabilization Rh nanoparticles against sintering [23]. Thus, the Rh/CeO<sub>2</sub>-NR/Al<sub>2</sub>O<sub>3</sub> catalyst is able to enhance the stability up to 70 h. In

Fig. 4. TEM images of (A) Rh/CeO<sub>2</sub>-NC, (B-C) Rh/CeO<sub>2</sub>-NC/Al<sub>2</sub>O<sub>3</sub>, (D) Rh/CeO<sub>2</sub>-NR and (E-F) Rh/CeO<sub>2</sub>-NR/Al<sub>2</sub>O<sub>3</sub> catalysts.

Fig. 5. TEM images of Rh/CeO<sub>2</sub>/Al<sub>2</sub>O<sub>3</sub> catalyst.Fig. 6. Steam reforming of PG conversion over Rh/CeO<sub>2</sub>–NR, Rh/CeO<sub>2</sub>–NC, Rh/CeO<sub>2</sub>–NR/Al<sub>2</sub>O<sub>3</sub>, Rh/CeO<sub>2</sub>–NC/Al<sub>2</sub>O<sub>3</sub> and Rh/CeO<sub>2</sub>/Al<sub>2</sub>O<sub>3</sub> catalysts.

contrast, Rh/CeO<sub>2</sub>/Al<sub>2</sub>O<sub>3</sub> catalyst exhibits a decrease in conversion after 20 h already. In this case, the irregular shaped CeO<sub>2</sub> nanoparticles of (111) plane formed on Al<sub>2</sub>O<sub>3</sub> by direct impregnation method, leading to a lower surface, lower absolute concentration of oxygen vacancies and less activated sites. It is well known that the CeO<sub>2</sub>–NRs and CeO<sub>2</sub>–NCs were enclosed by the {(110) and (100)} and (100) planes, while the ceria nanoparticles were enclosed by (111) planes [53]. When CeO<sub>2</sub> deposited on Al<sub>2</sub>O<sub>3</sub>, the surface energy and concentration of active sites are greater on (110) and (100) planes than for (111) planes of CeO<sub>2</sub> nanoparticles. Moreover, the (110) and (100) surface is more beneficial to produce oxygen vacancies and more catalytically active than (111) surfaces of irregular shaped ceria nanoparticles present on the alumina in Rh/CeO<sub>2</sub>/Al<sub>2</sub>O<sub>3</sub> catalyst. The high oxygen vacancy of CeO<sub>2</sub> NRs and NCs on Al<sub>2</sub>O<sub>3</sub> produce more oxygen mobility by reduction of Ce<sup>4+</sup> to Ce<sup>3+</sup> and react with deposited carbon on active Rh and keeps it active for a longer time period for CeO<sub>2</sub>–NR/Al<sub>2</sub>O<sub>3</sub> and CeO<sub>2</sub>–NC/Al<sub>2</sub>O<sub>3</sub> supported Rh catalysts compared to Rh/CeO<sub>2</sub>/Al<sub>2</sub>O<sub>3</sub>. The prolonged time of stability is also due to excellent sintering resistance of tiny Rh nanoparticles, which reduces the carbon deposition. The observed results proved that the rate of PG conversion and catalyst stability is mainly depending on the morphology of nanocrystalline CeO<sub>2</sub>.

Fig. 7 shows the selectivity towards the main product hydrogen as determined under conditions of steam reforming of propylene glycol for all the catalysts. All of the catalysts show high selectivity of hydrogen. The Rh/CeO<sub>2</sub>–NR catalyst possesses 82% of H<sub>2</sub> selectivity while Rh/CeO<sub>2</sub>–NC shows 63%. The possible explanation could be the difference

Fig. 7. H<sub>2</sub> selectivity over Rh/CeO<sub>2</sub>–NR, Rh/CeO<sub>2</sub>–NC, Rh/CeO<sub>2</sub>–NR/Al<sub>2</sub>O<sub>3</sub>, Rh/CeO<sub>2</sub>–NC/Al<sub>2</sub>O<sub>3</sub> and Rh/CeO<sub>2</sub>/Al<sub>2</sub>O<sub>3</sub> catalysts.

in dispersion of Rh nanoparticles over CeO<sub>2</sub> support. The theoretical work of Sayle and co-workers [32] have shown that the formation energies for anion vacancies is higher for (110) plane than (100) plane. The higher amount of anion vacancies of CeO<sub>2</sub> NRs may assist in stabilization of the Rh species leading to increase the Rh dispersion, which would be expected to provide higher number of accessible Rh sites, resulting in higher selectivity of H<sub>2</sub>. The H<sub>2</sub> selectivity remained constant during 100 h of time on stream for both the catalysts. Divins et al. [38] revealed the higher selectivity of hydrogen over CeO<sub>2</sub> nanorods and nanocubes supported RhPd catalysts than polycrystalline ceria based RhPd catalyst in steam reforming of ethanol at high temperature. However, the selectivity of hydrogen was maximum 60% which is lower than the present results. Ilgaz Soykal et al. [36] reported that the Co catalysts supported on ceria, which is preferentially exposing (110) plane possess better reforming catalysts for ethanol, resulting high yields for H<sub>2</sub> and CO<sub>2</sub>. The Rh/CeO<sub>2</sub>–NR/Al<sub>2</sub>O<sub>3</sub> and Rh/CeO<sub>2</sub>–NC/Al<sub>2</sub>O<sub>3</sub> catalysts underwent a decrease of hydrogen selectivity with increase of time on stream due to increase of by-products of CO, CO<sub>2</sub>, CH<sub>4</sub>, C<sub>2</sub>H<sub>4</sub> and C<sub>3</sub>H<sub>8</sub> (Fig. S4). The overall decrease in selectivity on Rh/CeO<sub>2</sub>–NR/Al<sub>2</sub>O<sub>3</sub> and Rh/CeO<sub>2</sub>–NC/Al<sub>2</sub>O<sub>3</sub> catalysts is probably due to part of Rh nanoparticles irregularly dispersed on Al<sub>2</sub>O<sub>3</sub> support with weak interaction and offered the less number of accessible Rh active sites. It is worth mentioning that Rh/CeO<sub>2</sub>/Al<sub>2</sub>O<sub>3</sub> catalyst shows the fluctuation in the production distribution. This implied that the irregular shape CeO<sub>2</sub> nanoparticles formed on alumina and less dispersion of Rh nanoparticles mainly affecting the product selectivity. This study demonstrates that the exposed crystal planes of CeO<sub>2</sub> play a key role in increase the catalyst stability and hydrogen selectivity.

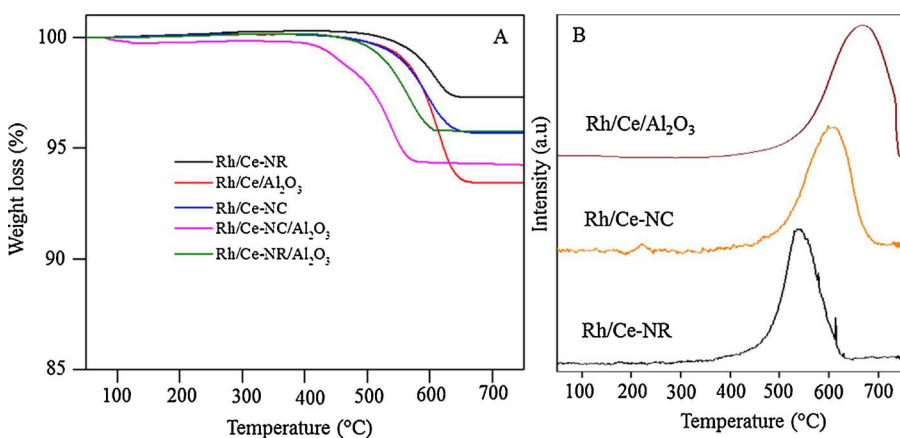
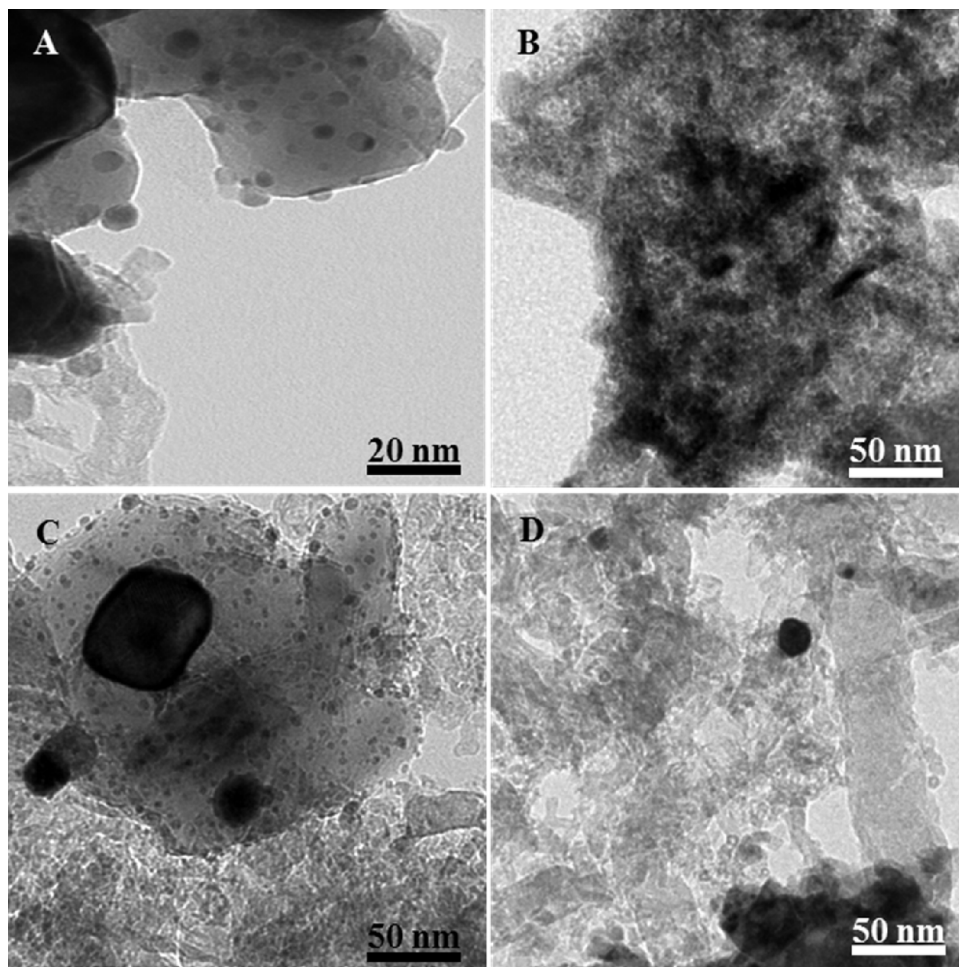


Fig. 8. (A) TGA and (B) TPO of spent catalysts.

### 3.3. Carbon analysis

In order to examine the possible carbon deposition and its effect on catalyst deactivation during the steam reforming reaction, various characterization techniques were applied on the spent catalysts. First, thermogravimetric analysis (TGA) was used to quantify the carbon deposition on all the spent catalysts after 100 h of reforming reaction time and results are shown in Fig. 8A. All the catalysts exhibit a weight loss at higher temperature ( $\sim 600$  °C) is attributed to the decomposition of graphitic carbon, which is further confirmed with TEM measurement (Fig. 9). The overall weight losses on Rh/CeO<sub>2</sub>-NR, Rh/CeO<sub>2</sub>-NC, Rh/CeO<sub>2</sub>-NR/Al<sub>2</sub>O<sub>3</sub>, Rh/CeO<sub>2</sub>-NC/Al<sub>2</sub>O<sub>3</sub> and Rh/CeO<sub>2</sub>/Al<sub>2</sub>O<sub>3</sub> are about

2.7%, 3.9%, 4.3%, 5.6% and 6.7%, respectively. The CeO<sub>2</sub>-NRs supported Rh catalyst shows much less carbon deposition when compared to the other catalysts, indicating that the ceria morphology significantly affected the amount of carbon deposition. Wang et al. [28] reported that asymmetrical five coordinated unstable oxygen with largest strain in CeO<sub>2</sub> NR was favorable for the mobility of surface oxygen, which would suppress the coke deposition leading to an enhanced catalytic stability. It is important to note that the maximum carbon deposition on Rh/CeO<sub>2</sub>/Al<sub>2</sub>O<sub>3</sub> was about 6.7%. Recently, we used mesoporous silica supported Ni catalysts for PG reforming reaction and those catalyst showed a higher amount of coke deposition and lost their stability in 30 h of time on stream [20]. The lower amount of carbon deposited on

Fig. 9. TEM images of spent (A) Rh/CeO<sub>2</sub>-NC, (B) Rh/CeO<sub>2</sub>-NR, (C) Rh/CeO<sub>2</sub>-NC/Al<sub>2</sub>O<sub>3</sub> and (D) Rh/CeO<sub>2</sub>-NR/Al<sub>2</sub>O<sub>3</sub> catalysts.

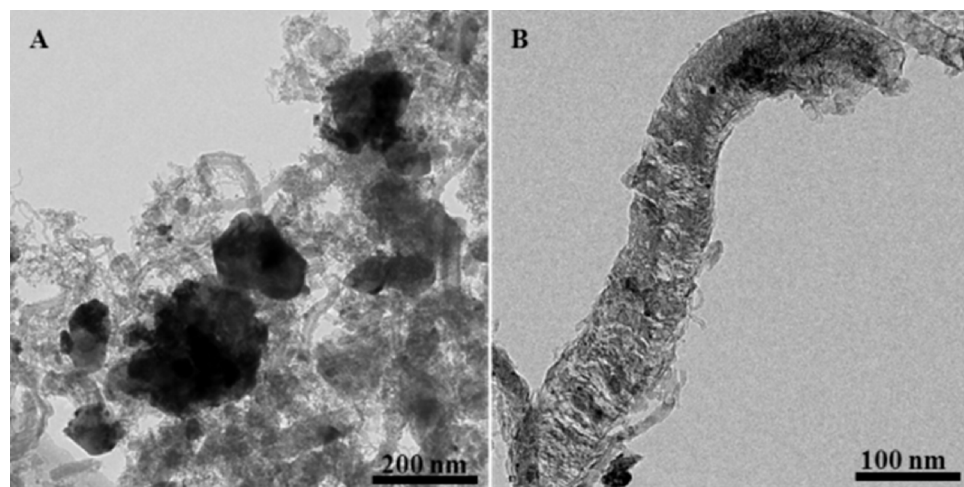


**Fig. 10.** TEM images of spent Rh/CeO<sub>2</sub>/Al<sub>2</sub>O<sub>3</sub> catalyst.

the surface of the catalysts used in this study is ascribed to the oxygen storage capacity of ceria, which aids the gasification of deposited carbon over active sites by activating the oxidation-reduction cycle. The TPO profiles obtained after the PG reforming over different catalysts are displayed in Fig. 8B. All the catalysts exhibit the single peak in the temperature range of 500–700 °C, which can be assigned to the decomposition of graphitic carbon deposited on the catalysts.

Fig. 9 shows the TEM images of spent Rh/CeO<sub>2</sub>–NR, Rh/CeO<sub>2</sub>–NC, Rh/CeO<sub>2</sub>–NR/Al<sub>2</sub>O<sub>3</sub> and Rh/CeO<sub>2</sub>–NC/Al<sub>2</sub>O<sub>3</sub> catalysts. The TEM images provide the evidence that negligible amount of carbon deposited on CeO<sub>2</sub>–NC and CeO<sub>2</sub>–NR supported Rh catalysts. The high mobile oxygen of CeO<sub>2</sub>–NR and CeO<sub>2</sub>–NC, is associated with the oxidation state between Ce<sup>4+</sup>/Ce<sup>3+</sup> by reversibly storing/releasing oxygen, may react with carbon deposits on Rh species and inhibiting the carbon accumulation. Interestingly, no apparent signs of Rh nanoparticles sintering were observed and the morphology of NRs and NCs has not been changed under the harsh reaction conditions at high temperature. The rhodium can interact with ceria forming Rh–O–Ce bonds which inhibit the sintering of rhodium particles in O<sub>2</sub>-containing atmosphere. The obtained results suggest that the strong interaction of Rh and CeO<sub>2</sub> effectively prevented the sintering of the highly dispersed Rh particles and the enhanced oxygen storage-release capacity of ceria greatly facilitated the coke gasification. In the case of Rh/CeO<sub>2</sub>/Al<sub>2</sub>O<sub>3</sub> catalyst (Fig. 10) the amount of carbon deposition was observed to be comparatively higher which might result from the lack of oxygen vacancies of the irregularly shaped CeO<sub>2</sub> particles present on alumina. Based on the above characterization observation, the catalysts deactivation factors can be deduced. The large number of oxygen vacancies and higher oxygen mobility on the CeO<sub>2</sub> NRs and NCs helped to resist the carbon formation and simultaneously enhanced the catalysts stability. Thus, the catalytic properties mainly depend on the shape and exposed crystal plane of the CeO<sub>2</sub> support.

#### 4. Conclusions

In this work, two different morphologies of CeO<sub>2</sub> supports were synthesized by a hydrothermal method and they were also deposited on to  $\alpha$ -Al<sub>2</sub>O<sub>3</sub>. The developed CeO<sub>2</sub> and CeO<sub>2</sub>/Al<sub>2</sub>O<sub>3</sub> were used as supports to prepare Rh-based catalysts for steam reforming of propylene glycol in microreactors. The characterization results prove that different morphologies provides different coordination environments and electronic states, which have great influence on the dispersion of Rh nanoparticles and the formation of oxygen vacancies exhibited a significant effect on the propylene glycol reforming reaction. It was found that the dispersion of Rh nanoparticles is improved on shape controlled CeO<sub>2</sub> NRs and NCs compared to CeO<sub>2</sub>/Al<sub>2</sub>O<sub>3</sub> suggesting that the lattice

perturbation of ceria resulted in better stabilization of Rh nanoparticles under reforming condition. The Rh/CeO<sub>2</sub>–NR and Rh/CeO<sub>2</sub>–NC catalysts exhibit higher conversion of PG and hydrogen selectivity and they were found to be stable up to 100 h owing to the better dispersion of Rh, the strong anchoring effect of CeO<sub>2</sub> to Rh, and sufficient mobile oxygen supply, which was favorable for the elimination of carbon deposition. The synthesis of morphology controlled CeO<sub>2</sub> could be a promising support to develop more stable catalysts for other reactions.

#### Acknowledgements

This work was supported by the Netherlands Center for Multiscale Catalytic Energy Conversion (MCEC), an NWO Gravitation programme funded by the Ministry of Education, Culture and Science of the government of the Netherlands (Grant number:10019185). The authors thank Mr. Nickolay Kosinov and M.W.G.M. (Tiny) Verhoeven for assistance in TGA and XPS experiments.

#### Appendix A. Supplementary data

Supplementary data associated with this article can be found, in the online version, at <https://doi.org/10.1016/j.apcatb.2017.12.062>.

#### References

- V. Shanmugam, S. Neuberg, R. Zapf, V. Hessel, G. Kolb, *Catal. Commun.* 83 (2016) 43–47.
- G. Kolb, V. Hessel, *Chem. Eng. J.* 98 (2004) 1–38.
- G. Kolb, *Chem. Eng. Process.* 65 (2013) 1–44.
- M. Pan, Q. Wu, L. Jiang, D. Zeng, *Appl. Energy* 154 (2015) 416–427.
- M. Mahmoudizadeh, A. Irankhah, R. Irankhah, M. Jafari, *Chem. Eng. Technol.* 39 (2016) 322–330.
- T. Hou, S. Zhang, T. Xu, W. Cai, *J. Chem. Engg.* 255 (2014) 149–155.
- D. Mei, M. Qian, B. Liub, B. Jin, Z. Yao, Z. Chen, *J. Power Sources* 205 (2012) 367–376.
- W. Cai, F. Wang, A. van Veen, C. Descorme, Y. Schuurman, W. Shen, C. Mirodatos, *Int. J. Hydrogen Energy* 35 (2010) 1152–1159.
- O. Görke, P. Pfeifer, K. Schubert, *Appl. Catal. A: Gen.* 360 (2009) 232–241.
- P.O. Vargas, C.H. Campos, R.M. Navarro, J.L.G. Fierro, P. Reyes, *J. Mol. Catal. A: Chem.* 407 (2015) 169–181.
- U.E. Salma Amjad, A. Vita, C. Galletti, L. Pino, S. Specchia, *Ind. Eng. Chem.* 52 (2013) 15428–15436.
- P.O. Graf, B.L. Mojet, J.G. van Ommen, L. Lefferts, *Appl. Catal. A: Gen.* 332 (2007) 310–317.
- M. Tóth, E. Varga, A. Oszkó, K. Baán, J. Kiss, A. Erdohelyi, *J. Mol. Catal. A: Chem.* 411 (2016) 377–387.
- C. Sun, H. Liab, L. Chen, *Energy Environ. Sci.* 5 (2012) 8475–8505.
- H. Cordatos, T. Bunlesuin, J. Stubenrauch, J.M. Vohs, R.J. Gortem, *J. Phys. Chem.* 100 (1996) 785–789.
- J. Kugai, V. Subramani, C. Song, M.H. Engelhard, Y.H. Chin, *J. Catal.* 238 (2006) 430–440.
- T. Montini, M. Melchionna, M. Monai, P. Fornasiero, *Chem. Rev.* 116 (2016) 5987–6041.

[18] R.B. Duarte, O.V. Safonova, F. Krumeich, M. Makosch, J.A. van Bokhoven, *ACS Catal.* 3 (2013) 1956–1964.

[19] A. Trovarelli, *Catal. Rev.: Sci. Eng.* 38 (1996) 439–520.

[20] V. Shanmugam, R. Zapf, S. Neuberg, V. Hessel, G. Kolb, *App. Catal. B: Environ.* 203 (2017) 859–869.

[21] J. Thormann, L. Maier, P. Pfeifer, U. Kunz, O. Deutschmann, K. Schubert, *Int. J. Hydrogen Energy* 34 (2009) 5108–5120.

[22] N.R. Peela, A. Mubayi, D. Kunzru, *Chem. Eng. J.* 167 (2011) 578–587.

[23] A.M. da Silva, K.R. de Souza, G. Jacobs, U.M. Graham, B.H. Davis, L.V. Mattos, F.B. Noronha, *Appl. Catal. B: Environ.* 102 (2011) 94–109.

[24] T. Montini, L. De Rogatis, V. Gombac, P. Fornasiero, M. Graziani, *Appl. Catal. B: Environ.* 71 (2007) 125–134.

[25] H.S. Roh, Y. Wang, D. King, *Top. Catal.* 49 (2008) 32–37.

[26] Y. Li, X. Wang, C. Song, *Catal. Today* 263 (2016) 22–34.

[27] W.I. Hsiao, Y.S. Lin, Y.C. Chen, C.S. Lee, *Chem. Phys. Lett.* 441 (2007) 294–299.

[28] N. Wang, W. Qian, W. Chu, F. Wei, *Catal. Sci. Technol.* 6 (2016) 3594–3605.

[29] Y. Zhang, Y. Yu, H. He, *Catal. Sci. Technol.* 6 (2016) 3950–3962.

[30] R. Wang, Y. Wang, M. Ren, G. Sun, D. Gao, Y.R.C. Chong, X. Li, G. Chen, *Int. J. Hydrogen Energy* 42 (2017) 6757–6764.

[31] H.X. Mai, L.D. Sun, Y.W. Zhang, R. Si, W. Feng, H.P. Zhang, H.C. Liu, C.H. Yan, *J. Phys. Chem. B* 109 (2005) 24380–24385.

[32] D.C. Sayle, S.A. Maicaneanu, G.W. Watson, *J. Am. Chem. Soc.* 124 (2002) 11429–11439.

[33] Z.P. Liu, S.J. Jenkins, D.A. King, *Phys. Rev. Lett.* 94 (2005) 196102–196104.

[34] Z. Yang, T.K. Woo, M. Baudin, K. Hermansson, *J. Chem. Phys.* 120 (2004) 7741–7749.

[35] Y. Jiang, J.B. Adams, M.v. Schilfgaarde, *J. Chem. Phys.* 123 (2005) (064701–064701).

[36] I. Ilgaz Soykal, B. Bayram, H. Sohn, P. Gawade, J.T. Miller, U.S. Ozkan, *Appl. Catal. A: Gen.* 449 (2012) 47–58.

[37] W. Hong, Z. Lijuan, L. Miao, L. Yuan, B. Xue, *J. Rare Earths* 31 (2013) 565–571.

[38] N.J. Divins, A. Casanova, W. Xu, S.D. Senanayake, D. Wiater, A. Trovarelli, J. Llorca, *Catal. Today* 253 (2015) 99–105.

[39] X. Du, D. Zhang, L. Shi, R. Gao, J. Zhang, *J. Phys. Chem. C* 116 (2012) 10009–10016.

[40] L.J. Liu, Z.J. Yao, Y. Deng, F. Gao, B. Liu, L. Dong, *ChemCatChem* 3 (2011) 978–989.

[41] X.S. Huang, H. Sun, L.C. Wang, Y.M. Liu, K.N. Fan, Y. Cao, *Appl. Catal. B: Environ.* 90 (2009) 224–232.

[42] M.L. Zhang, J. Li, H. Li, Y. Li, W. Shen, *Catal. Today* 148 (2009) 179–183.

[43] E. Aneggi, D. Wiater, C. de Leitenburg, J. Llorca, A. Trovarelli, *ACS Catal.* 4 (2013) 172–181.

[44] T. Désaunay, G. Bonura, V. Chiodo, S. Freni, J.P. Couzinié, J. Bourgon, A. Ringuedé, F. Labat, C. Adamo, M. Cassir, *J. Catal.* 297 (2013) 193–201.

[45] T.S. Moraes, R.C.R. Neto, M.C. Ribeiro, L.V. Mattos, M. Kourtelesis, X. Verykios, F.B. Noronha, *Top. Catal.* 58 (2015) 281–294.

[46] R. Zapf, C. Becker-Willinger, K. Berresheim, H. Bolz, H. Gnaser, V. Hessel, G. Kolb, P. Löb, A.-K. Pannwitt, A. Ziogas, *Chem. Eng. Res. Des.* 81 (2003) 721–729.

[47] G. Kolb, R. Zapf, V. Hessel, H. Löwe, *Appl. Catal. A: Gen.* 277 (2004) 155–166.

[48] U. Izquierdo, M. Wichert, G. Kolb, V.L. Barrio, R. Zapf, A. Ziogas, S. Neuberg, P.L. Ariasa, J.F. Cambra, *Int. J. Hydrogen Energy* 39 (2014) 5248–5256.

[49] M. Romeo, K. Bak, J. El Fallah, F. Le Normand, L. Hilaire, *Surf. Interface Anal.* 20 (1993) 508–512.

[50] A. Gayen, K.R. Priolkar, P.R. Sarode, V. Jayaram, M.S. Hegde, G.N. Subbanna, S. Emura, *Chem. Mater.* 16 (2004) 2317–2328.

[51] P.K. Sharma, N. Saxena, P.K. Roy, A. Bhatt, *Int. J. Hydrogen Energy* 41 (2016) 6123–6133.

[52] M. Nolan, S.C. Parker, G.W. Watson, *Surf. Sci.* 595 (2005) 223–232.

[53] J. Ren, X. Liu, R. Gao, W.L. Dai, *J. Energy Chem.* 26 (2017) 681–687.